A Nonlinear Kinematic Model for Film-Laminated Soft Bellows Actuators With Motion–Deformation Regime Transition

Yuzhou Duan, *Student Member, IEEE*, Jie Ling, *Member, IEEE*, Zuoqing Yu, and Yuchuan Zhu, *Member, IEEE*

***Abstract*—Soft bellows actuators (SBAs) driven by fluid power are increasingly explored for robotic systems operating in confined and contact-sensitive environments. Compared with mold-cast or glued SBAs, film-laminated SBAs achieve millimeter-scale dimensions and large elongation ratios; however, their axial kinematics exhibit pronounced nonlinearity due to the coupled effects of geometric motion and elastic deformation of laminated films. This Letter presents a regime-based, piecewise nonlinear kinematic model for film-laminated SBAs that decouples these effects by explicitly distinguishing two operating regimes: motion-dominated regime at low injection volumes and deformation-dominated regime at higher volumes. The transition between the two regimes is further incorporated into the modeling framework. The proposed model enables efficient and bidirectional prediction of nonlinear axial displacement from volume or pressure inputs, and vice versa. SBA prototypes are fabricated using a thin-film lamination process improved upon state-of-the-art techniques, in which thermosetting materials are employed as structural films with selective masking. This process results in ultra-small bonding regions (0.4 mm) and a millimeter-scale outer diameter (4.6 mm). Bench-top experiments on prototypes with different corrugation numbers demonstrate good agreement with the proposed model, with a maximum relative error of 9.31%, validating its accuracy and applicability.**

***Index Terms*—Soft sensors and actuators, micro/nano robots, bellows actuator, nonlinear modeling, soft fluidic actuator.**

I. Introduction

SOFT robots are distinguished by their intrinsic compliance, which enables safe and adaptive physical interaction with surrounding environments [1]. Their motion is typically achieved by pressurizing embedded chambers with air [2], liquid [3], or vacuum [4]. In such fluid-driven systems, actuation and structure are inherently coupled, blurring the distinction between actuator and robotic structure; here, we adopt the term *actuator* to describe an elementary fluid-driven soft robot. Among various soft actuators, the soft bellows actuator (SBA), characterized by a bellows-shaped chamber geometry, is one of the most prevalent and structurally efficient designs [5], [6], [7]. Its origami-inspired configuration primarily produces axial elongation under internal pressurization. While a single SBA exhibits a simple motion pattern, its modularity facilitates system-level integration: SBAs have been incorporated into continuum robots through serial [8], parallel [9], [10], and soft–rigid hybrid actuation schemes [11], enabling variable stiffness modulation, dexterous manipulation, and safe, adaptive interaction with unstructured environments.

Millimeter-scale SBAs have attracted increasing attention for microrobotic systems that require delicate and precise manipulation [12], [13]. Their compliance and elongation capability also make them suitable for minimally invasive surgical robots that must safely navigate narrow, tortuous anatomical lumens [14], [15]. However, reducing SBA size introduces significant fabrication challenges and increases demands on modeling accuracy. At this scale, monolithic molding is preferred over glue bonding due to the difficulty of uniform adhesive distribution and precise dosage control [16]. Casting remains feasible [12], but producing thin-walled bellows at the millimeter scale requires high mold accuracy and surface quality. High-precision 3D printing can mitigate some issues, yet surface texture and long-term reliability remain concerns. Machined molds offer precision and reliability but are costly and geometrically constrained [17].

Inspired by the “pop-up book microelectromechanical systems”[18], the film-laminated technique with heat and pressure is used to fabricate the millimeter-scale SBA. Rogatinsky et al. employed thermoplastic elastomer (TPE) as the structural layer and polytetrafluoroethylene (PTFE) as the mask layer to fabricate SBAs for cardiac interventions [14], [19]. The same technique was later applied by van Lewen et al. for bronchoscopy applications [15]. Building on this approach, Vo et al. incorporated a nylon mesh fabric film to enhance the structural layer strength and a heat-sealable nylon taffeta fabric to provide radial support for the multi-chamber SBA design [20]. Treadway et al. used thermoplastic polyurethane (TPU) ether films as the structural layer and glassine paper as the mask. However, at operating temperatures, both TPU and TPE can become liquid, which introduces challenges such as material leakage and over-melting, thereby limiting the achievable size, fabrication yield, and reproducibility. To overcome these limitations, Lee et al. developed an alternative approach using acrylic sheet adhesive (ASA) films to bond PTFE layers [13]. In this method, the PTFE

Received 12 January 2026; accepted 16 June 2026. Date of publication 28 August 2026; date of current version 8 September 2026. This article was recommended for publication by Associate Editor J. Liu and Editor X. Liu upon evaluation of the reviewers' comments. This work was supported in part by the National Natural Science Foundation of China under Grant 52505022, in part by the Fundamental Research Funds for the Central Universities under Grant NZ2026010, in part by the China University Industry-University-Research Innovation Fund under Grant 2025SR066, and in part by Outstanding Doctoral Dissertation in NUAA under Grant BCXJ25-10. *(Corresponding author: Jie Ling.)*

The authors are with the College of Mechanical & Electrical Engineering, Nanjing University of Aeronautics and Astronautics, Nanjing 210016, China (e-mail: dyz@nuaa.edu.cn; meejling@nuaa.edu.cn; meezqyu@nuaa.edu.cn; meeyczhu@nuaa.edu.cn).

This article has supplementary downloadable material available at https://doi.org/10.1109/LRA.2026.3728317, provided by the authors.

Digital Object Identifier 10.1109/LRA.2026.3728317

2377-3766 © 2026 IEEE. All rights reserved, including rights for text and data mining, and training of artificial intelligence and similar technologies.
Personal use is permitted, but republication/redistribution requires IEEE permission. See https://www.ieee.org/publications/rights/index.html for more information.

thorized licensed use limited to: NANJING UNIVERSITY OF AERONAUTICS AND ASTRONAUTICS. Downloaded on September 08,2026 at 06:30:31 UTC from IEEE Xplore. Restrictions appl

requires chemical surface modification via H_2 plasma to achieve strong and reliable bonding.

Apart from manufacturing considerations, various modeling methods have been developed to describe the behavior of SBAs including phenomenological models [21], [22], [23], geometric-based models [5], [24], and continuum models [25], [26]. Among these models, phenomenological models are simple and computationally efficient but lack predictive capability beyond fitted data, and these models require accurate identification of a relatively large number of parameters to ensure predictive accuracy. Geometric-based models capture structural kinematics across different SBA designs but often rely on simplifying assumptions and require calibration. Continuum models offer high accuracy for complex nonlinear deformations but are computationally intensive and demand extensive parameter identification. These approaches highlight the trade-off between simplicity, accuracy, and practicality, motivating advanced models that balance these factors.

Most existing modeling approaches have been developed for mold-cast or glued SBAs with dimensions on the order of tens of centimeters. In contrast, film-laminated SBAs exhibit significantly stronger nonlinearity due to the coupled effects of geometric motion and elastic deformation during axial elongation, making traditional models insufficient [13], [14]. Moreover, many film-laminated SBAs are fabricated at the millimeter scale, imposing stringent requirements on modeling accuracy. Current efforts for modeling film-laminated SBAs are predominantly geometric-based, as exemplified by the models proposed by Treadway et al. [27] and Rogatinsky et al. [19]. However, these models generally fail to capture the pronounced nonlinearity of film-laminated SBAs and exhibit limited generalizability. Continuum models that explicitly incorporate thin-film mechanics, although potentially accurate, are challenging to formulate and computationally expensive, limiting their practical applicability.

In this Letter, we present a regime-based, piecewise nonlinear kinematic model for film-laminated SBAs, which decouples geometric motion and elastic deformation into two submodels: a motion-dominated submodel at low injection volumes and a deformation-dominated submodel at higher volumes. A transition criterion, derived from geometric considerations, integrates the two submodels into a unified piecewise framework. To simplify the second submodel based on thin-film mechanics, a linear volume—pressure relationship is assumed and experimentally validated, such that the overall nonlinear model depends on a single control parameter, the injected volume. SBA prototypes are fabricated using an improved thin-film lamination technique, and experiments on prototypes with varying corrugation numbers validate the accuracy, repeatability, and scalability of the proposed model. The main contributions of this Letter are summarized as:

- Proposal of a piecewise nonlinear kinematic model that explicitly distinguishes between motion-dominated and deformation-dominated regimes, enabling accurate prediction of axial elongation in film-laminated SBAs.
- Derivation of an explicit criterion for regime transition and a verified volume–pressure assumption, yielding a unified model governed by a single control parameter while maintaining predictive accuracy.
- Development of an improved fabrication strategy that directly adopts thermosetting ASA films as structural layers, simplifying the fabrication process and reducing the film bonding regions.

II. Structure and Fabrication

The proposed SBA is a single-degree-of-freedom continuum actuator. As shown in Fig. 1(e), the actuator consists of a series of periodically arranged bellows-like chambers formed by laminated thin films, creating an enclosed and deformable structure. The actuator undergoes axial extension and contraction under fluidic actuation, with its deformation governed by the interaction between internal pressure and the laminated film structure. This hybrid configuration enables large deformation while preserving structural compliance.

The SBA is fabricated using a thin-film lamination process, wherein multilayer films are thermally pressed and selectively bonded in the direction normal to the film plane to form the configuration of the actuator (i.e., the bellows). The detailed fabrication procedure is described as follows.

As shown in Fig. 1(a), thin films made of different materials were patterned into different shapes using laser cutting technique. A femtosecond green laser (JL-1-JM3EC3, Juling Intelligent Technology Co., Ltd., China) was employed to achieve high edge quality in the patterned films, which is critical for reliable bonding. Two types of films were used to fabricate the SBA. Thermosetting films (B-staged modified ASA) served as the structural layers forming the bonded body of the SBA, while PTFE films were used as masks to define and regulate the selective bonding regions of the structural layers. Hereafter, these films are referred to as *structural films* and *mask films*, respectively, according to their functions.

In the next step (Fig. 1(b)), the patterned films are aligned and stacked within the molds using locating pins to ensure precise alignment. Rubber cushions are introduced to provide compliant contact among the films during the pressurization process. The assembled molds are subsequently placed into a hot-lamination machine for lamination (R3-3830P-50, Fuzhou Robco Intelligent Technology Co., Ltd., China). The process parameters were set to $200\,^{\circ}$C and 25 kPa in accordance with the material properties and empirical knowledge. The detailed lamination principle is depicted in Fig. 1(c). By alternately applying inner and outer mask films between the structural films, the inner and outer edges of the bellows were selectively bonded under hot pressing, while the regions designated to remain unbonded were isolated by the mask films. Furthermore, the number of bellows could be programmably defined.

After hot pressing, upper and lower end caps were fabricated via stereolithography (BIO resin, Wenext Co., Ltd., China) and attached to the bellows through glue bonding (LOCTITE 401 together with LOCTITE SF 770, Henkel Corp., USA.), as shown in Fig. 1(d). The lower end cap incorporated a hose barb for rapid connection to the hydraulic actuation system, whereas the upper end cap was designed to accommodate various functional modules, such as micro-grippers, miniature cameras, or optical fiber sensors, with proper sealing considerations. Following the attachment of the hose to the lower end cap and the purging of the internal air, the bellows could be hydraulically actuated. Finally, Fig. 1(e) presents a physical prototype fabricated using the aforementioned process, exemplified here with three corrugations. Compared with previous studies [19], [20], employing

thorized licensed use limited to: NANJING UNIVERSITY OF AERONAUTICS AND ASTRONAUTICS. Downloaded on September 08,2026 at 06:30:31 UTC from IEEE Xplore. Restrictions appl

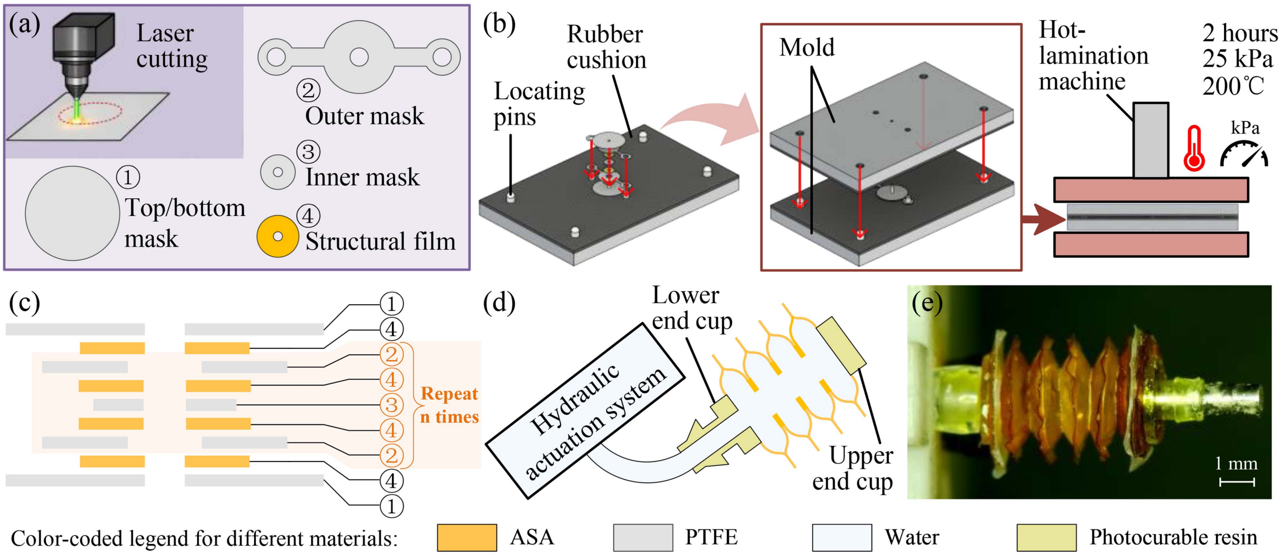

Fig. 1. Fabrication process of the soft bellows actuator (SBA). (a) Films are precisely patterned by laser cutting. (b) The patterned films are stacked in a mold and accurately aligned using locating pins. The mold is then closed and placed into a hot-lamination machine at a temperature of 200 °C and a pressure of 25 kPa for 2 h. (c) The detailed stacking order of the films selectively bonded to form the SBA. (d) After demolding, the upper and lower end caps fabricated by 3D printing are bonded to the laminated films, enabling hydraulic actuation of the SBA. (e) An example of the fabricated SBA prototype with three corrugations. Abbreviations: ASA, acrylic sheet adhesive; PTFE, polytetrafluoroethylene.

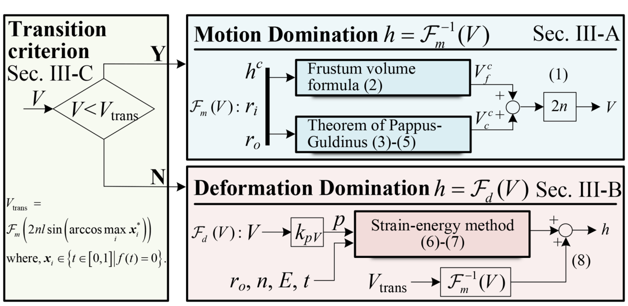

Fig. 2. The proposed model framework, including motion-dominated model (blue block), deformation dominated model (red block), and the transition criterion (green block).

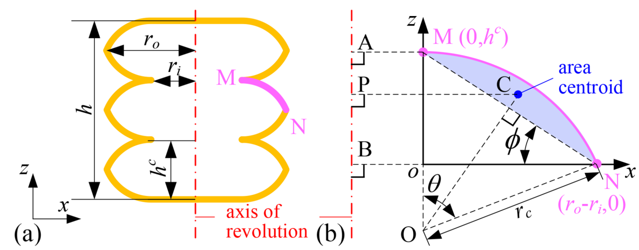

Fig. 3. Model diagram of the Soft bellows actuator (SBA). (a) Planar diagram of an SBA with three corrugations; (b) local Cartesian coordinate frame established along the curve MN for analytical geometry.

a thermosetting material as the structural film eliminates bonding errors induced by the flow of thermoplastic melts during hot pressing, thereby reducing the minimum bonding pitch to 0.4 mm. In comparison with [13], the structural films in this work are directly formed from ASA films, rather than PTFE films. This design choice simplifies the fabrication process by eliminating the need for chemical surface modification of PTFE films using H_2 plasma, which otherwise requires specialized and costly equipment.

III. Proposed Modeling Framework

Due to the variations in corrugation constraint conditions, the nonlinear kinematic model is formulated as a piecewise function consisting of two sub-models and the model transition criterion, as presented in Fig. 2. Submodel I, referred to as the *motion-dominated model*, describes the regime in which the bellows deformation is primarily governed by geometric motion. Once the injection volume reaches a critical value V_{trans}, the model transitions to submodel II, named the *deformation-dominated model*, in which the axial elongation is mainly attributed to the elastic deformation of the film. Fig. 3 presents the model diagram of the SBA. The following assumptions are adopted in the proposed model:

1) Ideal motion and unit uniformity assumption. Parasitic motions of the SBA outside the z-axis, as well as rotations about the z-axis, are neglected. All corrugations of the SBA are assumed to be identical.
2) Geometric assumptions. The outer wall of the corrugation (MN) is assumed to be a circular arc segment, with the center of the corresponding curvature circle located on the z-axis. The valley diameter r_i and peak diameter r_o of the corrugation remain constant.
3) Linear pressure–volume relationship. A linear relationship between the input pressure and the internal volume is assumed, as reported in [19] as well as further experimentally validated in Fig. 5.

Based on Assumption 1), the analysis can be restricted to a single corrugation, from which the behavior of the entire SBA

thorized licensed use limited to: NANJING UNIVERSITY OF AERONAUTICS AND ASTRONAUTICS. Downloaded on September 08,2026 at 06:30:31 UTC from IEEE Xplore. Restrictions appl

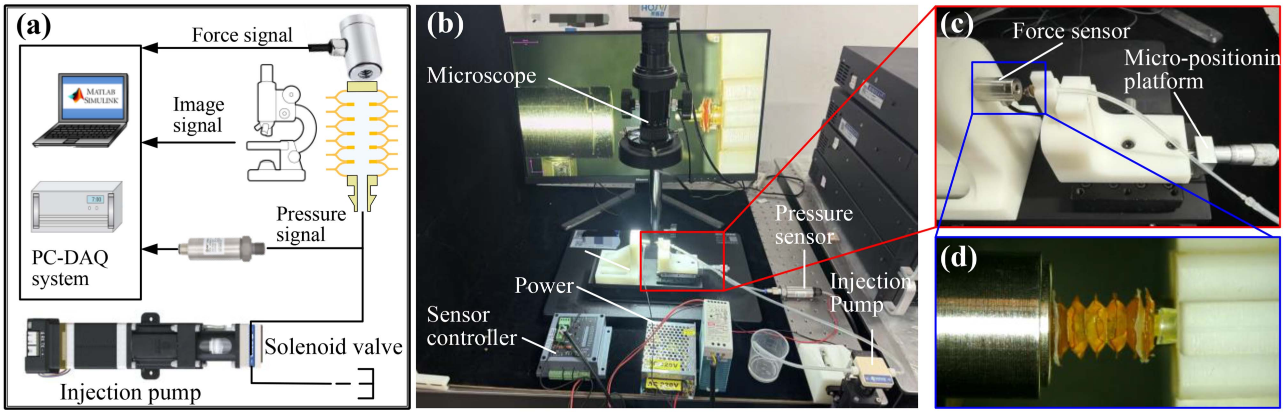

Fig. 4. Overview of the experimental system and the physical prototype: (a) schematic of the experimental setup; (b) photograph of the experimental system; (c) enlarged view of the physical prototype; (d) microscopic image of the soft bellows actuator.

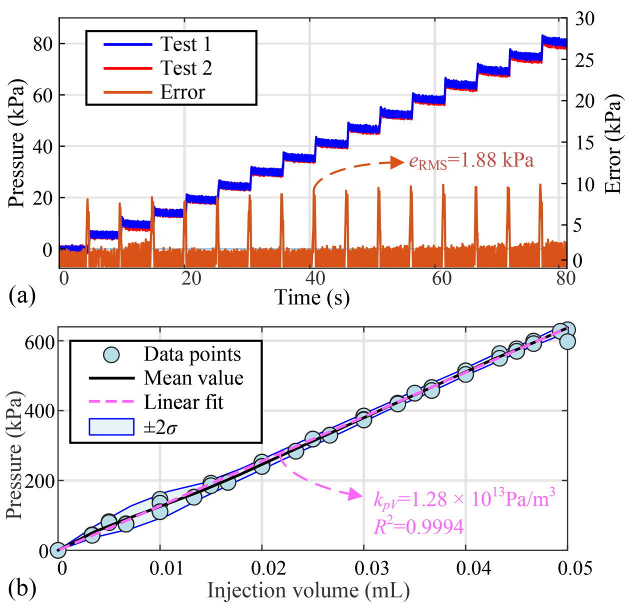

Fig. 5. Characterization of the pressure–volume relationship of the SBA. (a) Stepwise injection experiment with a dwell time of 5.4 s to ensure a steady state of the internal pressure. (b) Pressure–volume relationship obtained from experiment and the linear fitting results.

can be obtained and modeled. Accordingly, the volume and axial displacement in the whole model section are denoted by $V_{\bullet}^{c}$ and h^c for a single corrugation, whereas the corresponding total quantities without superscripts represent the entire SBA. The relationship between the two is given by $V_{\bullet} = nV_{\bullet}^{c}$ and $h = 2nh^c$, where n is the number of corrugations.

A. Submodel I: Motion-Dominated Model

For a single corrugation, the total volume of the internal cavity V^c can be regarded as the volume generated by revolving a planar region about the z-axis. As presented in Fig. 3, considering the symmetry, the revolved region can be decomposed into two contributions: one corresponding to twice the area of a trapezoid AMNB (generating double frustums), and the other to twice the area of a circular segment MN. The expression is shown as follows:

$$V = nV^c = 2n(V_f^c + V_c^c), \tag{1}$$

where V is the total injected volume, and V_f^c and V_c^c are the revolve-derived volumes of the trapezoid AMNB and the circular segment, respectively. Since V_f^c is the volume of a frustum, it can be further expressed as follows:

$$V_f^c = \frac{1}{3}\pi h^c \left(r_i^2 + r_o^2 + r_i r_o\right), \tag{2}$$

where h^c is half height of a corrugation. Assuming the radius of the circular segment is r_c, V_c^c can be derived according to the Theorem of Pappus-Guldinus:

$$V_c^c = 2\pi D A, \tag{3}$$

where the effective centroid distance D and cross-sectional area A can be derived from a sequence of geometric relations:

$$\begin{cases} c = \sqrt{(r_o - r_i)^2 + h^{c2}}, \\ d = \sqrt{r_c^2 - \frac{c^2}{4}}, \\ \theta = 2\arcsin\left(\frac{c}{2r_c}\right), \\ r_{\text{seg}} = \frac{4}{3} r_c \frac{\sin^3\left(\frac{\theta}{2}\right)}{\theta - \sin\theta}, \\ D = \frac{r_i + r_o}{2} + \frac{(r_{\text{seg}} - d)\, h^c}{c}, \\ A = r_c^2 \arctan\left(\frac{c}{2d}\right) - \frac{cd}{2}, \end{cases} \tag{4}$$

where, c is the length of MN, d is the perpendicular distance from the circle center O to MN, θ is the central angle corresponding to the chord MN, and r_{seg} is the distance from the centroid of the circular segment to the circle center (CO).

According to Assumption 2), r_c can be further derived as follows:

$$r_c(h^c) = \frac{(r_o - r_i)^2 + h^{c2}}{2h^c}. \tag{5}$$

By substituting (2)–(5) into (1) and noting that $h = 2nh^c$, the motion-dominated behavior can be derived and governed by a single parameter h, i.e., $\mathcal{F}_m : h \to V, 0 \leq V < V_{\text{trans}}$.

thorized licensed use limited to: NANJING UNIVERSITY OF AERONAUTICS AND ASTRONAUTICS. Downloaded on September 08,2026 at 06:30:31 UTC from IEEE Xplore. Restrictions appl

B. Submodel II: Deformation-Dominated Model

When the volume inside the chambers of the SBA reaches its maximum, the deformation-dominated model begins to lead the kinematics, where the elongation length is determined by the elastic deformation. This effect has been well studied. We adopt and modify Ref. [28] in this part, which derived a closed-form expression for the elongation length of a clamped circular film subjected to uniform pressure:

$$h = 2nh^c = 2n{r_o}^3\alpha\sqrt{\left(\frac{pr_o}{Et}\right)^3}, \tag{6}$$

where p is the uniform internal pressure, t is the film thickness, and E is the Young's modulus of the film material. The expression of α can be further represented by the Poisson ratio ν:

$$\alpha = \sqrt{\frac{6615(\nu^2-1)}{2\left(2791\nu^2-4250\nu-7505\right)^3}}. \tag{7}$$

According to Assumption 3), the input pressure can be expressed as $p = k_{pV}V/n$, where k_{pV} is an experimentally characterized pressure–volume proportionality constant. Therefore, when $V \geq V_{\text{trans}}$, the mapping $\mathcal{F}_d : V \to h$ can be analytically derived as follows (considering the initial length):

$$h = 2n{r_o}^3\alpha\sqrt{\left(\frac{Vk_{pV}r_o}{nEt}\right)^3} + \mathcal{F}_m^{-1}(V_{\text{trans}}). \tag{8}$$

C. Transition Criterion and Final Piecewise Model

In the previous two subsections, we established the motion-dominated and deformation-dominated kinematic models. The transition between these two models is governed by the volume in submodel I reaching its extremum V_{trans}. In practice, this transition occurs smoothly in the physical system, as also observed in the experimental results presented later. Here, however, we consider the idealized case and derive an analytical expression for V_{trans}. To obtain a computationally efficient expression for V_{trans} that can be directly evaluated from the geometric parameters, several assumptions are introduced. Assuming in submodel I the curvature radius corresponding to curve MN is much larger than the chord length, so the volumetric effect induced by the curvature can be neglected; and assuming the peak valley is a variable due to the wrinkling effect in the peripheral bonded region. By setting $V_c^c = 0$ and substituting $\phi = \arcsin(h^c/l) = \angle MNB$ in (1), one obtains

$$V(\phi) = \frac{2}{3}\pi nl\sin\phi\left(r_i^2 + (r_i + l\cos\phi)^2 + r_i(r_i + l\cos\phi)\right), \tag{9}$$

where $l = \bar{r_o} - r_i$. To identify the maximum of $V(\phi)$, consider the derivative of $V(t)$:

$$\mathrm{d}V/\mathrm{d}\phi \propto f(x), \qquad x = \cos\phi \in [0,1], \tag{10}$$

where

$$f(x) = 3l^2x^3 + 6r_il\,x^2 + (3r_i^2 - 2l^2)x - 3r_il, \quad r_i > 0,\ l > 0. \tag{11}$$

Evaluating $f(x)$ at the endpoints of [0,1] yields

$$\begin{aligned} f(0) &= -3r_il < 0, \\ f(1) &= l^2 + 3r_il + 3r_i^2 > 0. \end{aligned} \tag{12}$$

By the Intermediate Value Theorem, there exists at least one $x^* \in (0,1)$ such that

$$f(x^*) = 0. \tag{13}$$

Note that $h \in [0, l]$ implies $\phi \in [0, \pi/2]$ with a monotonic increase, whereas $\phi \in [0, \pi/2]$ implies $x \in [0,1]$ with a monotonic decrease. V_{trans} can be represented as follows:

$$V_{\text{trans}} = \mathcal{F}_m\left(2nl\sin\left(\arccos\max_i x_i^*\right)\right), \tag{14}$$

where $\{x_i^*\}$ are the roots of $f(x)$ in [0,1].

Finally, a regime-based piecewise model describing the nonlinear kinematics of the SBA is derived as follows:

$$h(V) = \begin{cases} \mathcal{F}_m^{-1}(V), 0 \leq V < V_{\text{trans}} \\ \mathcal{F}_d(V), V \geq V_{\text{trans}}. \end{cases} \tag{15}$$

D. Computational Cost Analysis

In addition to modeling capability, computational efficiency is critical for real-time implementation in soft robotic systems. To evaluate the efficiency of the proposed model, we measure its execution time in MATLAB for forward deformation computation over a full range of input volumes, covering both deformation regimes.

The computation is repeated 50 times to ensure statistical robustness. The results show that the total execution time is 3.87 $\pm$ 1.58 ms, corresponding to an average of approximately 0.019 ms per evaluation point. All computations are performed on a standard desktop computer equipped with an Intel i5-12400H CPU and 16 GB RAM using MATLAB R2021b.

This level of computational cost demonstrates that the proposed model is sufficiently efficient for real-time applications. Moreover, the model relies only on lightweight numerical root-finding and closed-form evaluations, avoiding complex iterative integration or high-dimensional parameter identification required in conventional continuum models.

IV. Experimental Characterization

A. Setups

The whole configuration of the experimental system is presented in Fig. 4. The signal flow of the experiments is shown in Fig. 4(a). A precision vertical injection pump (with resolution of 0.833 μL) together with a solenoid valve are employed to accurately control the injection volume of the SBA. A micro-force sensor (RDF-TM10, RYDER Co., Ltd., China) and a hydraulic pressure sensor (JPG23X5C1, UTMOST Co., Ltd., China) are introduced to measure the internal pressure and output force of the SBA. The displacement of the SBA is collected and derived through a microscope (AO-HD228SD, AOSVI Co., Ltd., China). The geometric and material parameters of the laminated SBA prototype are listed in Table I, where the material parameters are obtained from datasheets and experimental identification.

We use PC-based data acquisition system (Performance P3, Speedgoat Inc., Switzerland) to send control signals to the injection pump and collect sensor signals. The bench test is presented in Fig. 4(b), with an enlarged view of the main platform (Fig. 4(c)). A micro-positioning platform is used to adjust the distance between the robot and the force sensor. Fig. 4(d) shows the microscope view of the robot.

thorized licensed use limited to: NANJING UNIVERSITY OF AERONAUTICS AND ASTRONAUTICS. Downloaded on September 08,2026 at 06:30:31 UTC from IEEE Xplore. Restrictions appl

TABLE I
THE GEOMETRIC AND MATERIAL PARAMETERS OF THE PHYSICAL PROTOTYPE OF THE SBA

Parameter	Value	Parameter	Value
r_i	1.05 mm	n	3 & 5
r_o	1.95 mm	ν	0.3
V_{trans}	8.05e-3 mL	E	200 MPa

B. Volume–Pressure Relationship Characterization

To quantitatively characterize the volume–pressure relationship of the proposed SBA, a stepwise injection experiment was performed on two different prototypes. As illustrated in Fig. 5(a), the injected volume was increased from 0 to 0.05 mL (normalized to a single corrugation) with uniform increments, and a dwell time of 5.2 s was introduced at each step to ensure that the internal pressure reached a steady state. For each prototype, the experiment was repeated two times to evaluate repeatability.

The resulting pressure–volume curves are summarized in Fig. 5(b), where a strong linear dependence between pressure and volume can be observed over the entire range. Linear regression yields a coefficient of determination of $R^2 = 0.9994$, confirming the validity of a linear pressure–volume assumption within the tested range. The average standard deviation across repeated trials was 7.57 kPa, indicating good experimental consistency and robustness. Based on the fitted results, the volume–pressure coefficient was identified as $k_{pV} = 1.28 \times 10^{13}\ \mathrm{Pa/m^3}$.

C. Stroke Characterization

The stroke of the SBA was characterized to validate the proposed kinematic model. For each prototype, the injected volume was incrementally increased from 0 to 0.05 mL (normalized to a single corrugation) in 20 equally spaced steps. At each step, the elongation displacement of the SBA was measured under the microscope, and the experiment was repeated three times per prototype to assess reproducibility.

Fig. 6 illustrates the displacement–volume relationship of the two SBA prototypes, together with the predictions of the proposed model for comparison. The results reveal a pronounced nonlinear relationship between the injected volume and the resulting displacement. The experiments demonstrate good repeatability, with an average standard deviation of 4.68×10^{-2} mm and 3.80×10^{-2} mm for two prototypes. The root-mean-square (RMS) error between the experimental measurements and the model predictions is 4.87×10^{-2} mm and 3.04×10^{-2} mm for three-corrugation and five-corrugation prototype; and the maximum model error (percentage) is 9.31% and 6.88%, respectively, indicating good agreement between the model and the experimental results.

D. Force Characterization

Although the primary focus of this Letter is the validation of the proposed nonlinear kinematic model, the blocking force of the SBA prototypes was also experimentally measured using a force sensor, reaching 0.316 N for the three-corrugation prototype and 0.426 N for the five-corrugation prototype.

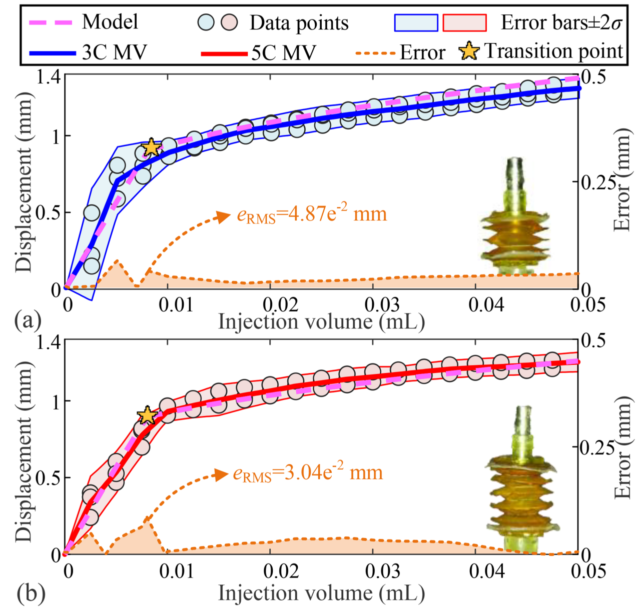

Fig. 6. Comparison of experimental results and model predictions for the volume–displacement relationship: (a) three-corrugation (3 C) prototype; (b) five-corrugation (5 C) prototype. Abbreviation: MV, mean value.

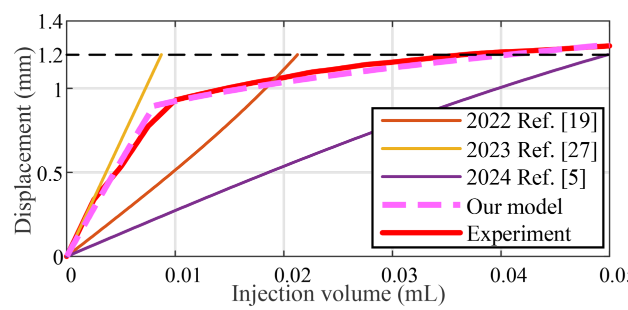

Fig. 7. Comparison between our kinematic models and other models for soft bellows actuators.

E. Comparison With Recent Works

To further clarify the contribution of the proposed model, a comparison is conducted with several recent kinematic models [5], [19], [27] for SBAs. As shown in Fig. 7, the kinematic models of our model, three reference models and the experimental data is presented together. We found that none of the three comparison models can accurately capture the nonlinear behavior. Among them, the model in [5] performs the worst, as the corresponding SBA is not film-laminated. The model in [19], identified using a fifth-order polynomial based on the SBA's intrinsic shape, exhibits limited generalizability. The single-parameter model proposed in [27], derived from a geometric approach under the constant-curvature assumption, agrees reasonably well with the initial portion of our Submodel 1 and the experimental data. However, it fails to describe the overall nonlinear elongation behavior of film-laminated SBAs. In contrast, the proposed regime-based model maintains good agreement with experimental results over the entire operating range by explicitly accounting for the shift from geometry-dominated motion to pressure-driven film deformation. This highlights the

thorized licensed use limited to: NANJING UNIVERSITY OF AERONAUTICS AND ASTRONAUTICS. Downloaded on September 08,2026 at 06:30:31 UTC from IEEE Xplore. Restrictions appl

TABLE II
COMPARISON OF REPRESENTATIVE BELLOWS ACTUATORS FABRICATED BY DIFFERENT METHODS

Reference	Year	Fabrication Method	Size	Stroke-Length Ratio	Stroke-Diameter Ratio	Output Force
Ref. [24]	2023	Mold Casting	33 mm	77%	16.7%	45 N
Ref. [11]	2023	Adhesive Bonding	30 mm	≈200%	40%	≈20 N
Ref. [13]	2024	Film-lamination	11.5 mm	305.9%	45.22%	4.49 N
This work	2026	Film-lamination	**4.6 mm**	**1653%**	27.0%	0.43 N

advantage of the proposed formulation in balancing modeling accuracy, physical interpretability, and computational simplicity.

In addition to kinematic accuracy, the practical advantages of the proposed fabrication method are also experimentally validated. Although the detailed design and manufacturing process are not the central focus of this work, a prototype SBA was fabricated following the described film-lamination procedure to assess its real-world viability. To date, film-laminated SBAs remain relatively rare in the literature. Therefore, a comparison is made between the fabricated prototype and several representative SBAs from recent studies, including those based on cast molding and adhesive bonding. As summarized in Table II, the film-laminated method enables a substantially smaller characteristic size (down to sub-centimeter scale) while achieving a larger elongation ratios (i.e. the stroke-length ratio in this Table) compared to most existing techniques. Moreover, owing to the improved fabrication method and material selection, the prototype presented in this Letter achieves an ultra-high elongation ratio of 1653% and a small diameter of 4.6 mm.

V. DISCUSSIONS

The proposed nonlinear kinematic model, together with the modified fabrication strategies presented in this Letter for SBAs, addresses several limitations observed in existing film-laminated SBAs.

Fabrication Advantages and Prototype Performance: The film-laminated fabrication approach enables a bonding region as small as 0.4 mm, which is critical for reducing the overall size of the SBA. Based on the results from SBA prototypes with three and five corrugations, the use of thermosetting structural films effectively suppresses material flow during hot pressing, yielding improved geometric consistency and repeatability across prototypes. Coupled with the carefully selected materials, the fabricated SBA achieves an elongation ratio of up to 1653%.

Model Contribution and Regime Transition: From a modeling perspective, the proposed nonlinear kinematic model unifies geometric kinematics and pressure-driven film deformation within a single-parameter formulation. Unlike prior models developed for mold-cast SBAs or the simplified linear-like models for film-laminated SBAs, the present approach explicitly captures the regime transition from motion-dominated axial extension to deformation-dominated film inflation. This transition is particularly relevant for film-laminated SBAs.

Experimental Validation and Control Implications: The experimentally observed linear volume–pressure relationship justifies the use of a calibrated proportional coefficient for pressure estimation, significantly simplifying the forward model without compromising accuracy within the tested operating range. This property is advantageous for real-time control, as volume-based actuation commands can be directly mapped to elongation displacement. Furthermore, the stroke characterization indicates that the actuators exhibit stable and repeatable axial behavior, which is critical for deployment in confined anatomical environments such as distal pulmonary airways [29].

System-Level Integration Potential: Although this work focuses on the fabrication and modeling of a single SBA unit, the proposed actuator and kinematic model are directly applicable to system-level robotic implementations. Film-laminated SBAs with similar structures have been successfully integrated into robotic systems such as soft grippers, end-effectors, and minimally invasive medical devices [13], [15], [19], demonstrating their practical feasibility. The proposed model can serve as a plug-in kinematic module in model-based control and planning frameworks, due to its compact formulation and computational efficiency. In particular, the millisecond-level computation time enables real-time evaluation, which is essential for closed-loop control. Furthermore, multiple SBA units can be combined to construct multi-actuator systems (e.g., continuum manipulators), where the proposed model can be extended within standard piecewise or constant-curvature frameworks to predict overall kinematics.

Limitations and Future Work: Several limitations should be noted. The current model assumes axisymmetric deformation and neglects out-of-plane parasitic motions, which may occur under asymmetric loading or contact with surrounding tissues. In addition, viscoelastic effects and long-term material fatigue are not considered, which may influence performance under prolonged or cyclic operation and affect the fatigue life of the SBA. Finally, a kinetostatic model considering the influence of output force was not developed. Future work will focus on extending the model to incorporate environmental interactions and additional degrees of freedom, as well as to account for the rigid–soft fabrication effects in the hot-lamination process.

VI. CONCLUSION

This Letter proposed a regime-based nonlinear kinematic model for film-laminated SBAs. By explicitly distinguishing between geometry-dominated and deformation-dominated elongation mechanisms and introducing an analytical transition criterion, the proposed model accurately captures the strongly nonlinear volume–displacement relationship characterized in experiments. After employing an improved fabrication technique that adopts thermosetting ASA films as structural films to fabricate SBA prototypes, validation on SBA prototypes with three and five configurations demonstrates good prediction accuracy and repeatability of proposed model. The proposed modeling framework provides a physically interpretable and computationally efficient tool for the analysis and control of millimeter-scale film-laminated SBAs.

thorized licensed use limited to: NANJING UNIVERSITY OF AERONAUTICS AND ASTRONAUTICS. Downloaded on September 08,2026 at 06:30:31 UTC from IEEE Xplore. Restrictions appl

REFERENCES

[1] M. Li, A. Pal, A. Aghakhani, A. Pena-Francesch, and M. Sitti, "Soft actuators for real-world applications," *Nature Rev. Mater.*, vol. 7, pp. 235–249, 2022.

[2] A. Comoretto, H. A. Schomaker, and J. T. Overvelde, "Physical synchronization of soft self-oscillating limbs for fast and autonomous locomotion," *Science*, vol. 388, no. 6747, pp. 610–615, 2025.

[3] D. Du, E. Del Dottore, A. Mondini, E. Sinibaldi, and B. Mazzolai, "Modular growing mechanism with multi-axis deformation," in *Proc. 2024 IEEE Int. Conf. Robot. Automat.*, 2024, pp. 176–182.

[4] X. Wang et al., "Bionic soft fingers with hybrid variable stiffness mechanisms for multimode grasping," in *Proc. 2024 IEEE Int. Conf. Robot. Automat.*, 2024, pp. 1957–1963.

[5] Y. Qiu et al., "An MR-safe robotic manipulator with hydraulic bellows actuators for spine procedures," *IEEE/ASME Trans. Mechatron.*, vol. 29, no. 3, pp. 1785–1796, Jun. 2024.

[6] J. Zhou, Y. Chen, X. Chen, Z. Wang, Y. Li, and Y. Liu, "A proprioceptive bellows (PB) actuator with position feedback and force estimation," *IEEE Robot. Automat. Lett.*, vol. 5, no. 2, pp. 1867–1874, Apr. 2020.

[7] Z. Wang et al., "A soft robotic hand based on bellows actuators for dishwashing automation," *IEEE Robot. Automat. Lett.*, vol. 6, no. 2, pp. 2139–2146, Apr. 2021.

[8] H. Cheng, L. Chen, B. Fang, J. Zhang, and J. Hong, "Switching control for a soft rehabilitation glove with pneumatic bellows actuators," *IEEE Robot. Automat. Lett.*, vol. 9, no. 6, pp. 4966–4973, Jun. 2024.

[9] W. Zhu et al., "A soft-rigid hybrid gripper with lateral compliance and dexterous in-hand manipulation," *IEEE/ASME Trans. Mechatron.*, vol. 28, no. 1, pp. 104–115, Feb. 2023.

[10] S. Ku, B.-H. Song, T. Park, Y. Lee, and Y.-L. Park, "Soft modularized robotic arm for safe human-robot interaction based on visual and proprioceptive feedback," *Int. J. Robot. Res.*, vol. 43, no. 8, pp. 1128–1150, 2024.

[11] Z. Zhang et al., "Bioinspired rigid-soft hybrid origami actuator with controllable versatile motion and variable stiffness," *IEEE Trans. Robot.*, vol. 39, no. 6, pp. 4768–4784, Dec. 2023.

[12] S. Ahn, W. Jung, K. Ko, Y. Lee, C. Lee, and Y. Hwang, "Thermopneumatic soft micro bellows actuator for standalone operation," *Micromachines (Basel)*, vol. 12, no. 1, p. 46, 2021.

[13] H. C. Lee et al., "A fabrication strategy for millimeter-scale, self-sensing soft-rigid hybrid robots," *Nature Commun.*, vol. 15, no. 1, p. 8456, 2024.

[14] J. Rogatinsky et al., "A multifunctional soft robot for cardiac interventions," *Sci. Adv.*, vol. 9, no. 43, 2023, Art. no. eadi5559.

[15] D. Van Lewen, T. Janke, H. Lee, R. Austin, E. Billatos, and S. Russo, "A millimeter-scale soft robot for tissue biopsy procedures," *Proc. Adv. Intell. Syst.*, 2023, Art. no. 2200326.

[16] S. Zhang, X. Ke, Q. Jiang, Z. Chai, Z. Wu, and H. Ding, "Fabrication and functionality integration technologies for small-scale soft robots," *Adv. Mater.*, vol. 34, no. 52, 2022, Art. no. 2200671.

[17] M. A. Bell, K. P. Becker, and R. J. Wood, "Injection molding of soft robots," *Adv. Mater. Technol.*, vol. 7, no. 1, 2021, Art. no. 2100605.

[18] J. P. Whitney, P.S. Sreetharan, K. Y. Ma, and R. J. Wood, "Pop-up book MEMS," *J. Micromechanics Microengineering*, vol. 21, no. 11, 2011, Art. no. 115021.

[19] J. Rogatinsky et al., "A collapsible soft actuator facilitates performance in constrained environments," *Adv. Intell. Syst.*, vol. 4, no. 10, 2022, Art. no. 2200085.

[20] V. T. Vo et al., "Soft, fiber-reinforced bellow actuators," *IEEE Robot. Automat. Lett.*, vol. 10, no. 2, pp. 1896–1903, Feb. 2025.

[21] R. Hashem, M. Stommel, L. K. Cheng, and W. Xu, "Design and characterization of a bellows-driven soft pneumatic actuator," *IEEE/ASME Trans. Mechatron.*, vol. 26, no. 5, pp. 2327–2338, Oct. 2021.

[22] V. Falkenhahn, T. Mahl, A. Hildebrandt, R. Neumann, and O. Sawodny, "Dynamic modeling of bellows-actuated continuum robots using the euler–lagrange formalism," *IEEE Trans. Robot.*, vol. 31, no. 6, pp. 1483–1496, Dec. 2015.

[23] R. Hashem, S. Kazemi, M. Stommel, L. K. Cheng, and W. Xu, "A biologically inspired ring-shaped soft pneumatic actuator for large deformations," *Soft Robot.*, vol. 9, no. 4, pp. 807–819, 2022.

[24] K. K. Lin, Y. Qiu, K. Yan, Q. Ding, and S. S. Cheng, "Towards mr-safe concentric bellows-based hydrostatic linear actuator for a needle driver," in *Proc. 2023 IEEE/RSJ Int. Conf. Intell. Robots Syst., Conf. Proc.*, 2023, pp. 10252–10259.

[25] Z. Kan, C. Pang, Y. Zhang, Y. Yang, and M. Y. Wang, "Soft actuator with programmable design: Modeling, prototyping, and applications," *Soft Robot.*, vol. 9, no. 5, pp. 907–925, 2022.

[26] J. Liang, X. Huang, K. Luo, Z. Song, Y. Yang, and F. Chen, "Design and kinematic modeling of a pneumatic soft bellow-type wrist," *IEEE Robot. Automat. Lett.*, vol. 9, no. 7, pp. 6312–6319, Jul. 2024.

[27] E. Treadway, M. Brei, A. Sedal, and R. B. Gillespie, "A single-parameter model for soft bellows actuators under axial deformation and loading," in *Proc. 2023 IEEE/RSJ Int. Conf. Intell. Robots Syst., Conf. Proc.*, 2023, pp. 582–589.

[28] A. Hermida, "Deflection of circular membrane under differential pressure," *NASA Tech Briefs Mag.*, vol. 22, no. 5, p. 78, 1998.

[29] Y. Duan, J. Ling, M. Rakotondrabe, Z. Yu, L. Zhang, and Y. Zhu, "A review of flexible bronchoscope robots for peripheral pulmonary nodule intervention," *IEEE Trans. Med. Robot. Bionics*, vol. 7, no. 3, pp. 845–862, Aug. 2025.

thorized licensed use limited to: NANJING UNIVERSITY OF AERONAUTICS AND ASTRONAUTICS. Downloaded on September 08,2026 at 06:30:31 UTC from IEEE Xplore. Restrictions appl